AGU PUBLICATIONS

JGR

Journal of Geophysical Research: Atmospheres

RESEARCH ARTICLE

10.1002/2016JD025665

Key Points:

- This study demonstrates the predominant role of a global circumnavigating mode in MJO initiation and propagation
- There is little impact of whether or not the MJO signal retained in the initial conditions of the regional domain
- The removal of the global MJO signals from the boundaries does not affect the propagation of the MJO after MJO starts in regional domain

Correspondence to:

F. Zhang,
fzhang@psu.edu

Citation:

Zhang, F., S. Taraphdar, and S. Wang (2017), The role of global circumnavigating mode in the MJO initiation and propagation, *J. Geophys. Res. Atmos.*, *122*, 5837–5856, doi:10.1002/2016JD025665.

Received 17 OCT 2016
Accepted 26 MAY 2017
Accepted article online 31 MAY 2017
Published online 10 JUN 2017

The role of global circumnavigating mode in the MJO initiation and propagation

Fuqing Zhang[1], **Sourav Taraphdar**[1], **and Shuguang Wang**[2]

[1]Department of Meteorology and Atmospheric Science, and Center for Advanced Data Assimilation and Predictability Techniques, Pennsylvania State University, University Park, Pennsylvania, USA, [2]Department of Applied Physics and Applied Mathematics, Columbia University, New York, New York, USA

Abstract A series of convection-permitting regional-model simulations are used to study the influences of intraseasonal forcings from the periphery of the tropical Indian Ocean on the October 2011 Madden-Julian Oscillation (MJO) event well observed during the Dynamics of the Madden-Julian Oscillation field campaign. These sensitivity experiments demonstrate the predominant role of a global circumnavigating mode in the initiation and propagation of this MJO event, although the regional framework would not completely rule out influences from the extratropics through the western boundary of the model domain. It is found that filtering out intraseasonal forcing leads to the absence of Kelvin waves, which may reduce moisture transport and weakened lower level convergence at the leading edge of the westerlies and further leads to diminishing MJO signatures in these sensitivity experiments. Meanwhile, for the same regional domain initiated 2 weeks before the onset of the MJO convection, there is little impact of whether or not the global MJO signals retained in the initial conditions. On the other hand, the removal of the global MJO signals from the lateral boundary conditions will not affect the propagation of the MJO after it has been initiated in the regional model domain.

1. Introduction

The principal mode of tropical intraseasonal oscillations in the boreal winter is the Madden-Julian Oscillation (MJO) [*Madden and Julian*, 1971], which is also one of the primary sources of variability and predictability for global weather at lead periods lengthier than 2 weeks [*Zhang*, 2005; *Hoskins*, 2013; *Chi et al.*, 2015]. Challenges remain for the current weather and climate models to properly simulate and forecast the MJO initiation, maintenance, and propagation in particular over the Indo-Pacific region [e.g., *Seo et al.*, 2009; *Hung et al.*, 2013; *Jiang et al.*, 2015].

Different arguments have been proposed in the past to understand what specific processes lead to the MJO convection initiation and propagation in the Indian Ocean. For example, extratropical forcing via Rossby wave activities propagating to the low latitudes was hypothesized to initiate the MJO convection [*Lau and Peng*, 1987; *Lin et al.*, 2006], but existing modeling studies often have difficulties in unambiguously separating the extratropical forcing from the tropical mean state influence [e.g., *Ray and Li*, 2013; *Ray et al.*, 2009]. A recent study by *Ma and Kuang* [2016] managed to exclude the role of mean state changes when the influence of extratropical forcing is examined using a superparameterized community atmospheric model.

Strong cloud-radiative feedback in the Indian Ocean [e.g., *Lin et al.*, 2004] is found to play an important role in driving large variations in the surface fluxes, moisture advection, and moist static energy [e.g., *Maloney et al.*, 2010; *Sobel et al.*, 2010; *Sobel and Maloney*, 2012; *Sobel et al.*, 2014; *Pritchard and Bretherton*, 2014; *Johnson et al.*, 2015] for the MJO events observed during the Dynamics of the Madden-Julian Oscillation (DYNAMO) field campaign [*Yoneyama et al.*, 2013]. Importance of radiation [*Wang et al.*, 2013] for the MJO events and also its interactions with cloud for maintaining the vertical structure of large-scale velocity [*Wang et al.*, 2016] is also demonstrated using cloud-resolving model.

An alternative hypothesis attributes the MJO initiation to circumnavigating Kelvin waves. Many studies found that while the MJO convective signals are primarily manifest in the Indo-Pacific region [*Knutson and Weickmann*, 1987], upper tropospheric signals associated with the MJO (e.g., zonal wind and velocity potential) are continuous across the globe, suggesting that proceeding dry signals may be responsible for trigger of MJO convection in the Indian Ocean [*Kikuchi and Takayabu*, 2003; *Matthews*, 2008; *Ajayamohan et al.*, 2013]. However, the evidence from modeling experiments remains inconclusive to test the global circumnavigating mode hypothesis in the MJO initiation [*Ray and Li*, 2013; *Zhao et al.*, 2013; *Maloney and Wolding*, 2015; *Ma and Kuang*, 2016], which is at least partially due to deficiencies in parameterized convection to properly represent the observed MJOs in some of these modeling studies.

Building on the success of the control simulation of the October 2011 MJO event during DYNAMO presented in *Wang et al*. [2015, hereafter W15], the present study seeks to elucidate the role of global circumnavigating mode in the MJO initiation and propagation through a set of uniquely designed regional-scale convection-permitting numerical experiments. Evaluated against observations, W15 showed that the control simulation at 9 km horizontal grid spacing captured well the slow eastward propagation of the October MJO event in surface precipitation, outgoing longwave radiation, zonal wind, humidity, and large-scale vertical motion.

The rest of the sections are as follows. Data, methodology, and experimental design will be given in section 2. Results and discussions through analysis of various experiments on the importance of a global circumnavigating mode in the MJO initiation and propagation are presented in section 3. Section 4 gives the concluding remarks.

2. Experimental Design

The Weather Research and Forecasting (WRF) model version 3.4.1 [*Skamarock et al*., 2008] is used in the current study for the control simulation and sensitivity experiments with the horizontal domain covering the equatorial Indian Ocean from 20°S to 20°N and from 48° to 120°E at the 9 km grid spacing and with 45 stretched vertical levels. The control experiment (CNTL) follows exactly the same configurations as in W15 including using the same model physics and the same initial and boundary conditions provided by the 0.75° × 0.75° ERA-Interim global reanalysis [*Dee et al*., 2011]. The WRF model is initialized at 00 UTC 1 October 2011 integrated for 46 days in the free running mode, except for the first 3 days during which a large-scale spectral nudging is applied to the horizontal wind field only. The lower boundary forcings in terms of sea surface temperature (SST) are also updated every 6 h using the ERA-Interim SST. Please refer to W15 for details in the CNTL simulation configuration including specifics on the initial spectral nudging during the first 3 days.

The use of time-varying SST as lower boundary conditions is designed to produce time-evolving atmospheric states that are both internally consistent within the atmosphere and as consistent as possible with the observed atmospheric evolution during the simulation period. The time-varying SST, like the time-varying lateral boundary conditions, is a mathematically well-posed condition to help achieve such consistency with observations and model physics/numerics. Our simulations already incorporate time-varying lateral boundary conditions which are influenced by atmospheric observations from outside the domain. That exterior atmosphere is coupled to the atmosphere within the domain as much as the SST within the domain is; there is no fundamental difference between specifying these lateral boundary conditions and specifying the SST as a lower boundary condition.

The use of time-independent SST for the lower boundary condition (in place of more accurate 6-hourly SST), on the other hand, will likely lead to less consistency. Results from sensitivity experiments based on time-independent SST would require one to separate the effects of time-independent SST and altered lateral boundary conditions (as discussed below), which would unnecessarily complicate interpretation of sensitivity experiments, and less likely to be indicative of the underlying mechanisms of the MJO event in question.

Nevertheless, the effect of using time-varying versus time-independent SST on the simulated MJO was examined in W15 (their Figure 12): the use of time-independent SST did not affect the successful simulation of the DYNAMO October MJO event, suggesting that this event is primarily driven by the atmospheric dynamics [*Fu et al*., 2015], which are the subject of further examination in this study using the time-varying SST low boundary.

We design a set of sensitivity experiments to elucidate the roles of the global circumnavigating signals and extratropical forcing in initiating the DYNAMO October MJO event. These experiments are nearly identical to the CNTL simulation except for some modifications in the lateral boundary or initial conditions. Specifically, all state variables in either lateral or initial boundaries are bandpass filtered to deny potential external influences (Table 1): (i) both the initial and boundary conditions (NoMJO), (ii) only initial condition (NoMJOic), and (iii) only boundary conditions (NoMJObc). We apply a time-space filter following the *Wheeler and Kiladis* [1999, hereafter WK] to separate MJO signal from all fields in the ERA-Interim reanalysis

Table 1. Descriptions of Different Numerical Experiments Where MJO Filter Bands of Periods 20–96 Days and Wave Numbers of 1–9 Are Used

Experiments	Descriptions	Purpose
CNTL	Control simulation	For realistic representation of MJO initiation and propagation
NoMJOic	MJO filter applied to the initial condition only	Role of global circumnavigating mode when removed from only initial conditions
NoMJObc	MJO filter applied on the boundary condition only	Same as NoMJOic but when removed from only boundary conditions
NoMJO	MJO filter applied on both initial and boundary conditions	Same as NoMJObc but when removed from both initial and boundary conditions
NoMJObc1	Same as NoMJObc but MJO filter applied on 16 October onward instead of 1 October 2011	Importance of boundary conditions
NoMJObc2	Same as NoMJObc but MJO filter applied on 26 October onward instead of 1 October 2011	Further support for the importance of boundary conditions
NoMJOew	Same as NoMJO experiment but MJO filter applied only in the east-west boundary but not in north-south	Separate out the role of east-west boundary
NoMJOns	Same as NoMJO experiment but MJO filter applied only in the north-south boundary but not in east-west	Separate out the role of north-south boundary

before using it to generate the initial and boundary conditions for the WRF sensitivity experiments. Previous studies suggest the necessity of realistic boundary conditions for initiation and maintenances of MJO both in real [*Ray and Zhang*, 2010] and idealized [*Wedi and Smolarkiewicz*, 2010] conditions. Removal of MJO from the initial and boundary conditions was studied earlier by *Gustafson and Weare* [2004a, 2004b] using the Pennsylvania State University-National Center for Atmospheric Research MM5 model, but the current uses a spectral filter to accommodate both the spatial-temporal information including the direction (e.g., eastward or westward). Further experiments are added to isolate the importance of boundary conditions, similar to the NoMJObc experiments, but the MJO filter is applied on 16 October (NoMJObc1) and 26 October (NoMJObc2) onward instead of 1 October 2011 (Table 1). Additional experiments are also performed similarly to NoMJO, but the MJO band-pass filter is applied only in east-west boundaries but not in the north-south (NoMJOew) or vice versa (NoMJOns), respectively.

The MJO filter bands are set to from 20 to 96 days in time and from 1 to 9 in global zonal wave numbers here (as in *Fang and Zhang* [2016] and *Schreck et al*. [2011, 2012]). The MJO filter applied to all variables required to create the model initial and boundary conditions (e.g., three-dimensional zonal wind (U), meridional wind (V), temperature, relative humidity (RH), geopotential and for two-dimensional 10 m zonal (U10), meridional wind (V10), RH, surface pressure, mean sea level pressure, and skin temperature) in the ERA-Interim reanalysis data set for the above mentioned spatial and temporal bands. The filtered signals are then subtracted from the respective unfiltered ERA-Interim variables for experiments without MJO and further used to produce the required initial and lateral boundaries in the sensitivity experiments described above (i.e., NoMJO, NoMJOic, and NoMJObc). Figure 1 shows the time-longitude diagram of U850, U200, and RH850, (averaged over 5°S–5°N), from the unmodified ERA-Interim data set (Figures 1a, 1c, and 1e), and the MJO data (Figures 1b, 1d, and 1f), respectively. The latter shows clearly the eastward propagation of the MJO signal in all these variables at different levels, indicating that the time-space filter effectively separate the intraseasonal signals (Figures 1b, 1d, and 1f) as designed. Figure 2 illustrates the actual signals as well as what has been modified for U, V, and relative humidity at 850 hPa at the western boundary (i.e., 48°E) of the model domain in different numerical experiments. The filtered signal shows the initial intraseasonal propagation followed by initiation and propagation of MJO mode along the Indian Ocean.

The ERA-Interim reanalysis, 3 h surface rainfall from TRMM3B42 (version 7) [*Huffman et al*., 2007], and the satellite-based total precipitable water vapor estimated from Special Sensor Microwave Imager and Tropical Rainfall Measuring Mission Microwave Imager are all used for validation and comparisons of CNTL and sensitivity experiments.

3. Results and Discussions

3.1. Structural Evolution of MJO in the Sensitivity Numerical Experiments

Figure 3 displays the Hovmöller diagram of 3-hourly observational rainfall estimated by TRMM3B42 (Figure 3a) and the 850 hPa zonal wind (U850; shaded; m s^{-1}) from the ERA-Interim reanalysis overlapped

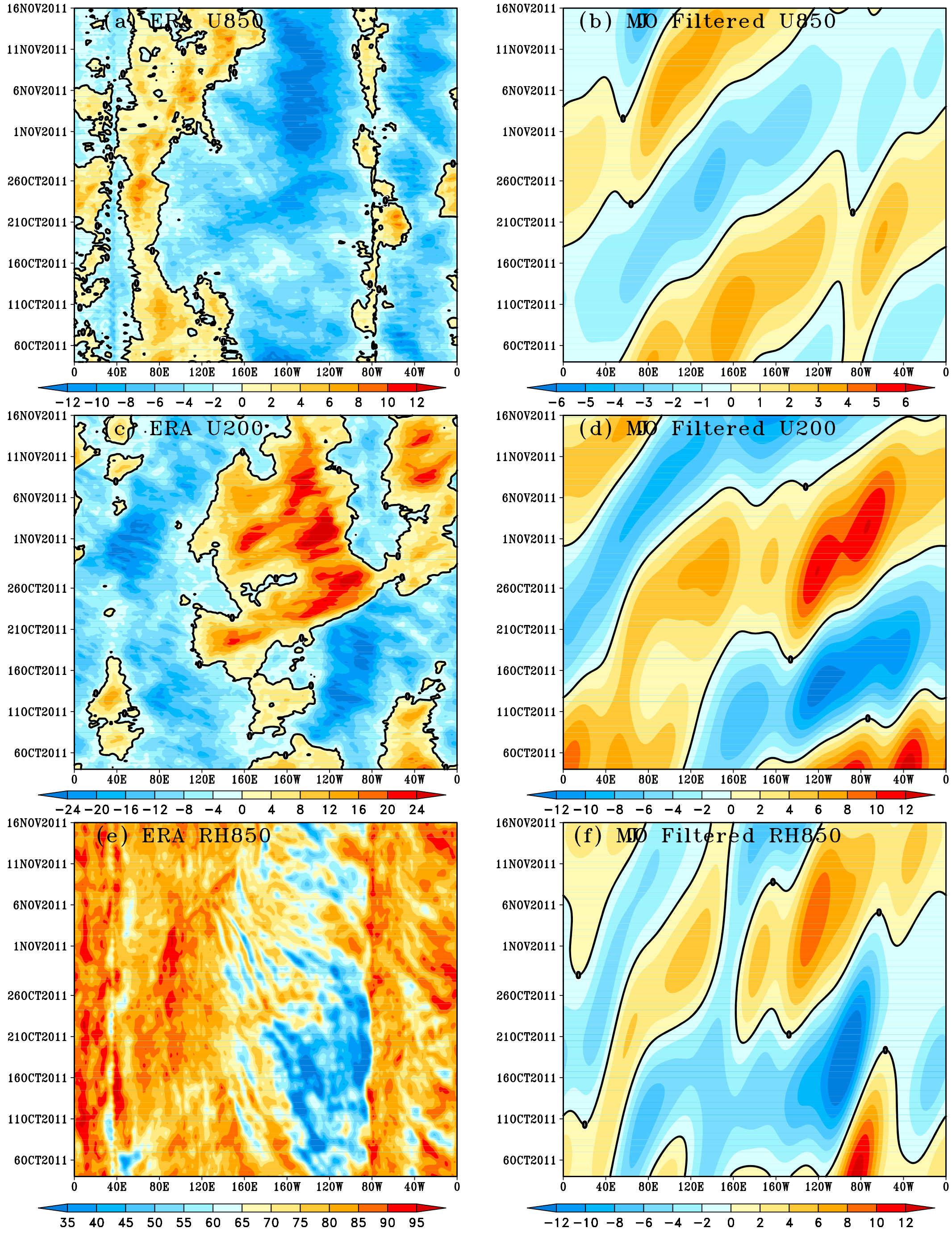

Figure 1. Time-longitude diagram of (a) 850 hPa zonal wind (m s^{-1}; U850), (b) MJO filtered U850, (c) 200 hPa zonal wind and (m s^{-1}; U200), (d) MJO filtered U200, (e) 850 hPa relative humidity (%; RH850), and (f) MJO filtered RH850 from ERA-Interim reanalysis data averaged over the latitude 5°S–5°N, respectively.

with the 15 mm d^{-1} daily Tropical Rainfall Measuring Mission (TRMM) precipitation (Figure 3b), averaged over the latitude band 5°S–5°N, respectively. The enhanced organized convective activities begin at ~60°E around 16 October, which propagate eastward with time, while disruption occurs near the Maritime Continent at ~100°E. Rainfall maximum associated with the MJO event collocates with the maximum low-level convergence in the leading edge of the westerlies (Figure 3b). The phase relationship between U850 and

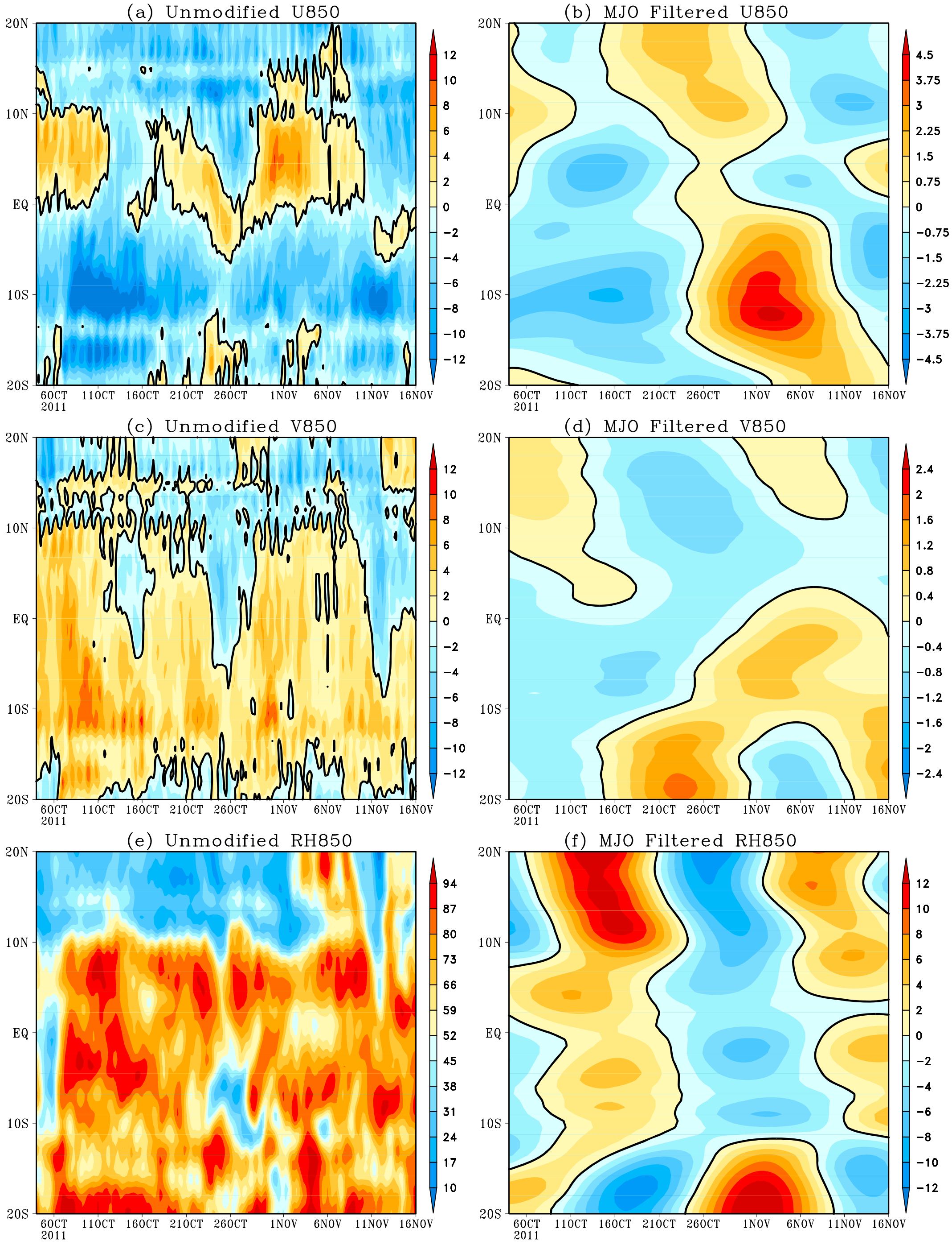

Figure 2. Time-latitude diagram of 850 hPa (a) zonal wind (m s^{-1}; U850), (b) MJO filtered U850, (c) meridional wind (m s^{-1}; V850), (d) MJO filtered V850, (e) relative humidity (%; RH850), and (f) MJO filtered RH850 from ERA-Interim reanalysis data at western boundary, i.e., at 48°E longitude.

rainfall is consistent with the conceptual MJO model proposed by *Madden and Julian* [1972]. The 3-hourly surface precipitation Hovmöller diagram from TRMM (Figure 3a) also shows apparent high-frequency variations including westward propagating signals during an active (moist) phase of the eastward propagating MJO. Abundant smaller-scale westward propagating waves are also prominent west of the Maritime Continent, likely originated from diurnal variations. The high-frequency variability can be better

(a) TRMM

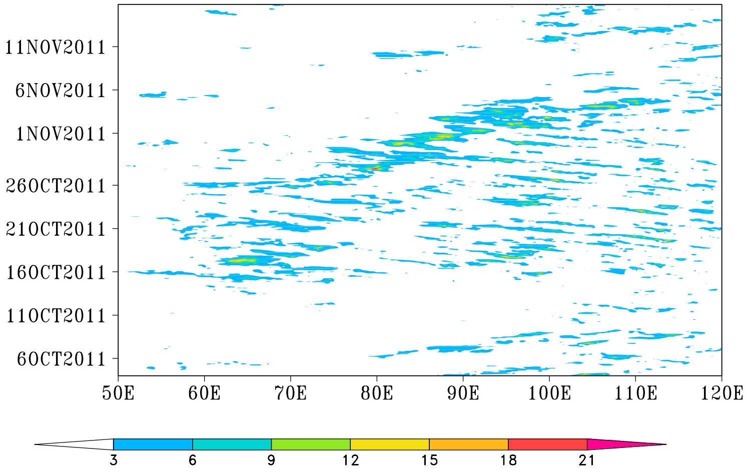

(b) ERA+TRMM

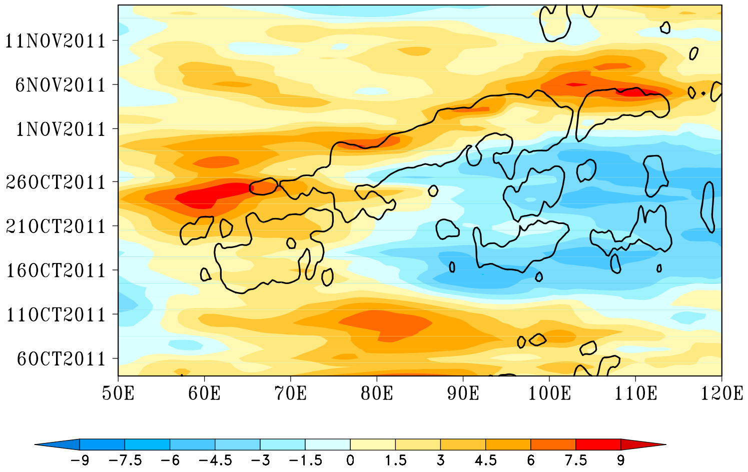

(c) TRMM

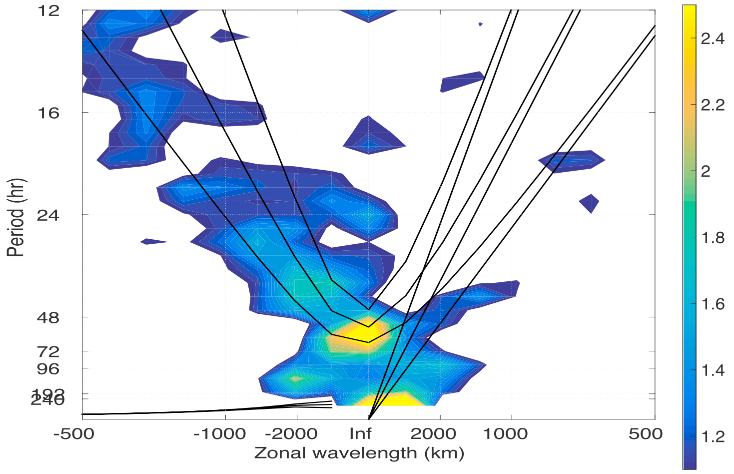

Figure 3. Time-longitude diagram of observed (a) 3-hourly precipitation (mm 3 hr^{-1}) from TRMM3B42 and (b) 850 hPa zonal wind (shaded; m s^{-1}) from ERA-Interim and daily TRMM3B42 precipitation (contour, 15 mm d^{-1}), averaged over the latitude 5°S–5°N, respectively. (c) The normalized symmetric spectrum of TRMM3B42 precipitation over Indian Ocean (50°–90°E) averaged between the latitude 5°S–5°N. The temporal window is 16 days, and temporal resolution is 3-hourly. Solid curve corresponds to $n = 1$ inertia-gravity waves and Kelvin waves with the equivalent depth of 12, 25, and 50 m.

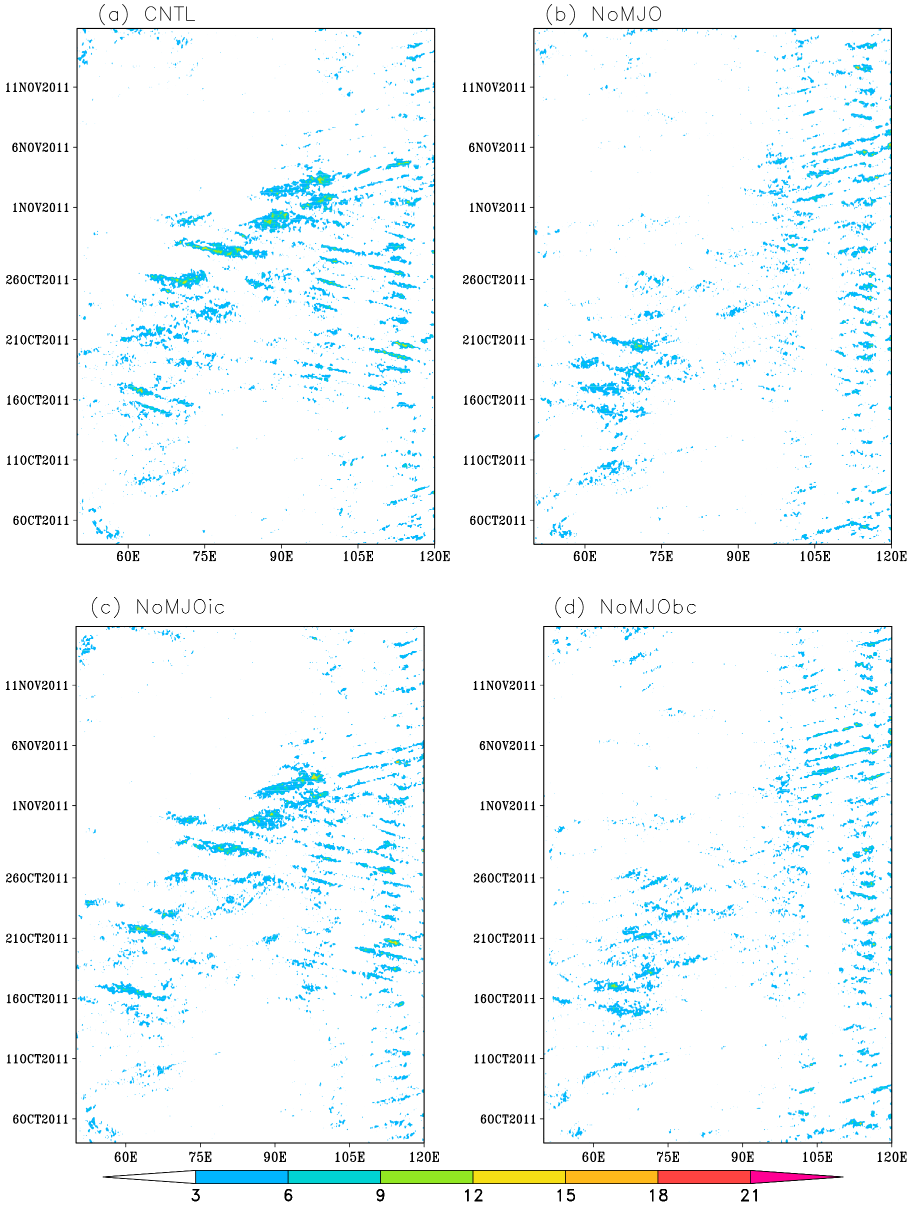

Figure 4. Time-longitude diagram of 3-hourly precipitation (mm 3 h^{-1}) from (a) CNTL simulation, (b) NoMJO, (c) NoMJOic, and (d) NoMJObc experiments averaged over the latitude 5°S–5°N, respectively.

quantified by the wave number-frequency diagram (see details in W15) of the 3-hourly surface rainfall (Figure 3c), a regional equivalent of the global Wheeler-Kiladis diagram. A Fourier transform of the 3-hourly rainfall in the longitude range 50°–90°E, averaged between 5°S and 5°N, is performed within a 16 day time section using 8 day overlapping segments. Low-frequency variabilities are not represented well mainly because of limited longitudinal and temporal windows for the regional model simulations. The primary features highlighted in TRMM precipitation are eastward propagating Kelvin waves and westward propagation of inertia-gravity waves.

As in TRMM, all simulations (Figure 4) show enhanced organized convection at ~60°E and around 16 October but only CNTL and NoMJOic are able to capture the eastward propagation of rainfall (and its disruption near the Maritime Continent ~100°E). Both CNTL and NoMJOic properly capture the MJO initiation around 16 October that resembles the observations, and its eastward propagation of the MJO is evident in the simulated 850 hPa zonal wind (Figure 5). MJO initiation from the global prospective often means a large-scale

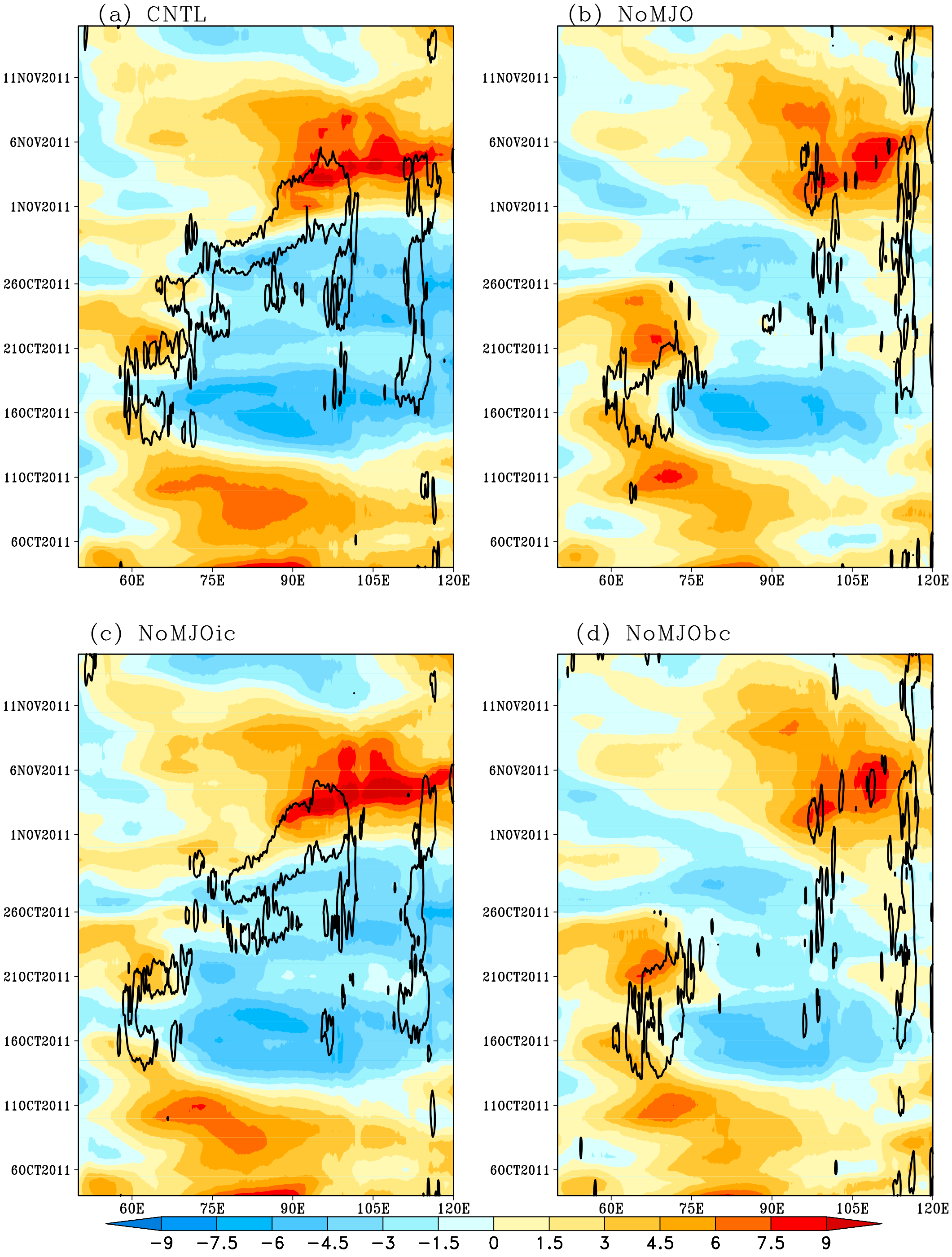

Figure 5. Time-longitude diagram of zonal wind at 850 hPa (shaded; m s^{-1}) and daily precipitation (contour; 15 mm d^{-1}) from (a) CNTL simulation, (b) NoMJO, (c) NoMJOic, and (d) NoMJObc experiments averaged over the latitude 5°S–5°N, respectively.

convective event has to sustain and propagate over an extended distance at a slow phase speed. Large-scale convective activities occur in the western Indian Ocean during 16 and 21 October in both the NoMJO and NoMJObc experiments (without the MJO mode in the lateral boundary conditions) but fail to propagate eastward; both experiments show breakdown of the eastward propagating low-level convergence during 26 October and 1 November (Figures 5b and 5d). The 3-hourly precipitation diagram (Figure 4) and the regional equivalent of the global Wheeler-Kiladis diagrams (Figure 6) from CNTL and NoMJOic are also

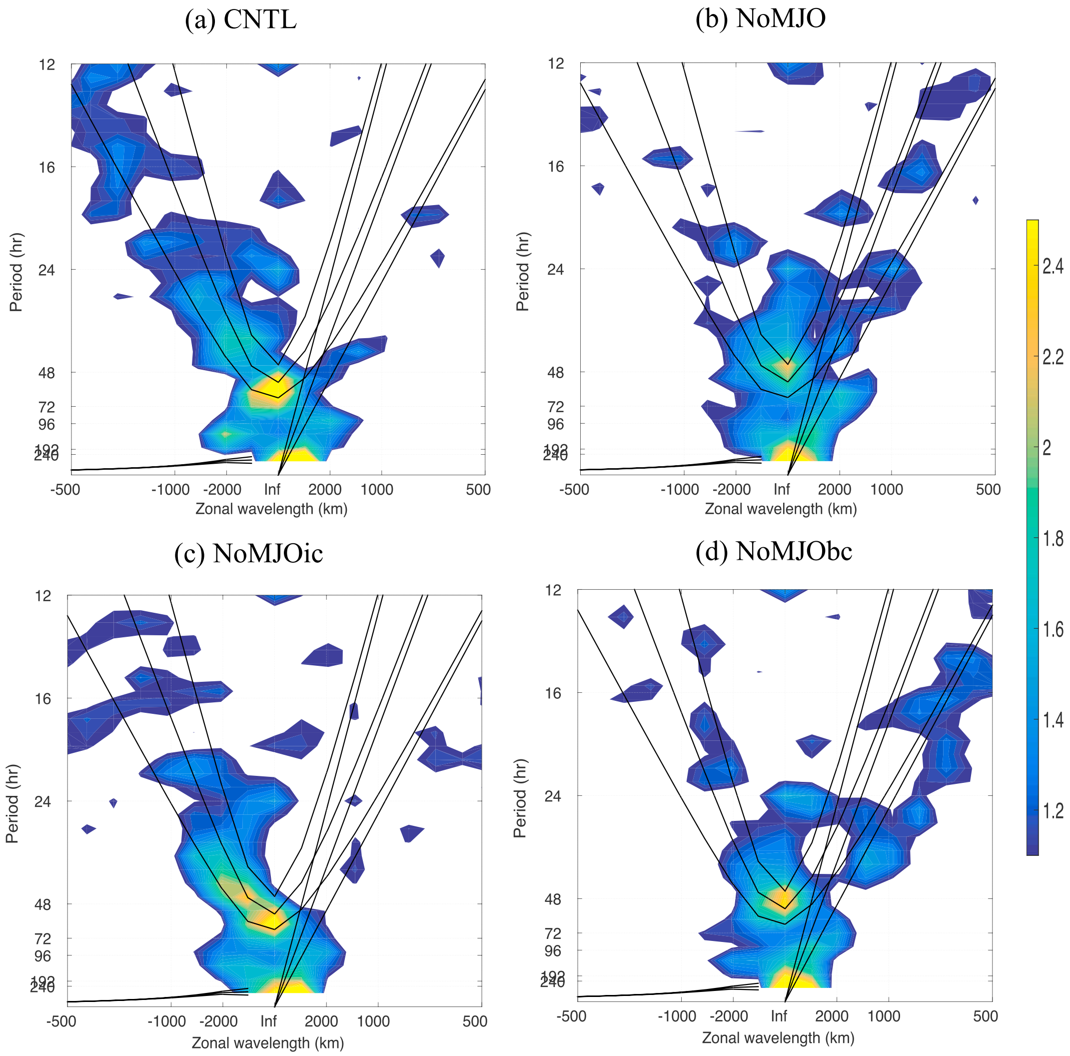

Figure 6. Normalized symmetric spectrum of precipitation over Indian Ocean (50°–90°E) averaged between 5°S and 5°N for (a) CNTL simulation, (b) NoMJO, (c) NoMJOic, and (d) NoMJObc experiments, respectively. The temporal window is 16 days, and temporal resolution is 3-hourly. Solid curve corresponds to $n = 1$ inertia-gravity waves and Kelvin waves with equivalent depth of 12, 25, and 50 m.

consistent with the observed patterns derived from the TRMM data set (Figure 3c) that capture the eastward propagation of Kelvin and westward propagation of inertia-gravity waves. However, without an apparent eastward propagating MJO, the other two sensitivity experiments (NoMJO and NoMJObc) fail to simulate the observed spectra of the westward propagating inertia-gravity waves (Figures 6b and 6d). Also, the apparent high-frequency variations including westward propagating signals during an active (moist) phase of the eastward propagating MJO is weaker in both the NoMJO and NoMJObc experiments (Figures 4b and 4d). Since both experiments without the MJO signals in lateral boundary conditions (NoMJO and NoMJObc) fail to simulate the MJO precipitation over the Indian Ocean while the other two experiments (CNTL and NoMJOic) do, it suggests that the global circumnavigating MJO mode from the model lateral boundaries (instead of in the initial conditions within the simulation domain) plays a prominent role in the initiation and propagation of the October MJO event during DYNAMO. To further support our above statement, we filter out the MJO signal from all the above simulations (i.e., NoMJOic, NoMJObc, and NoMJO) which is compared to the CNTL simulation. Figure 7 shows the Hovmöller diagram of the MJO filtered zonal wind at 850 hPa (shaded) and 200 hPa (contour) from all the above mentioned experiments averaged over latitude range of 5°S–5°N. The eastward propagation of MJO signal in both the upper and lower level is depicted well in the CNTL and NoMJOic experiments but not in NoMJO and NoMJObc where

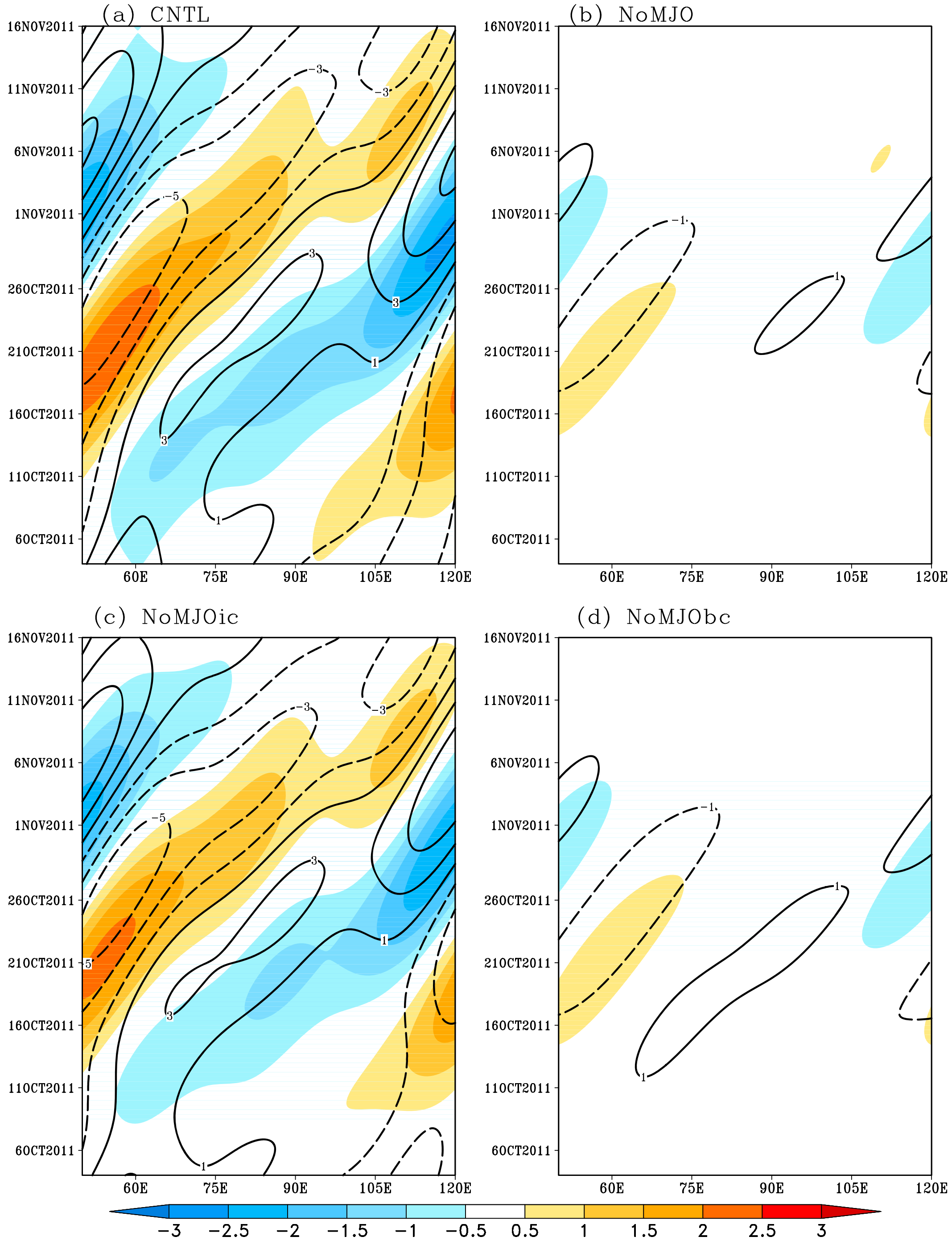

Figure 7. Time-longitude diagram of MJO (20–96 days; 1–9) filtered zonal wind at 850 hPa (shaded; m s^{-1}) and 200 hPa (contour; m s^{-1}) from (a) CNTL simulation, (b) NoMJO, (c) NoMJOic, and (d) NoMJObc experiments averaged over the latitude 5°S–5°N, respectively.

the propagation is not only weaker but also disrupted over 70°–75°E at around 21–23 October, suggesting that the global circumnavigating mode plays an important role for MJO initiation and propagation through the model lateral boundaries.

To further examine the differences in the MJO initiation and propagation among different experiments in comparison to the observations, Figure 8 displays the longitude-height cross section of the 3 day averaged

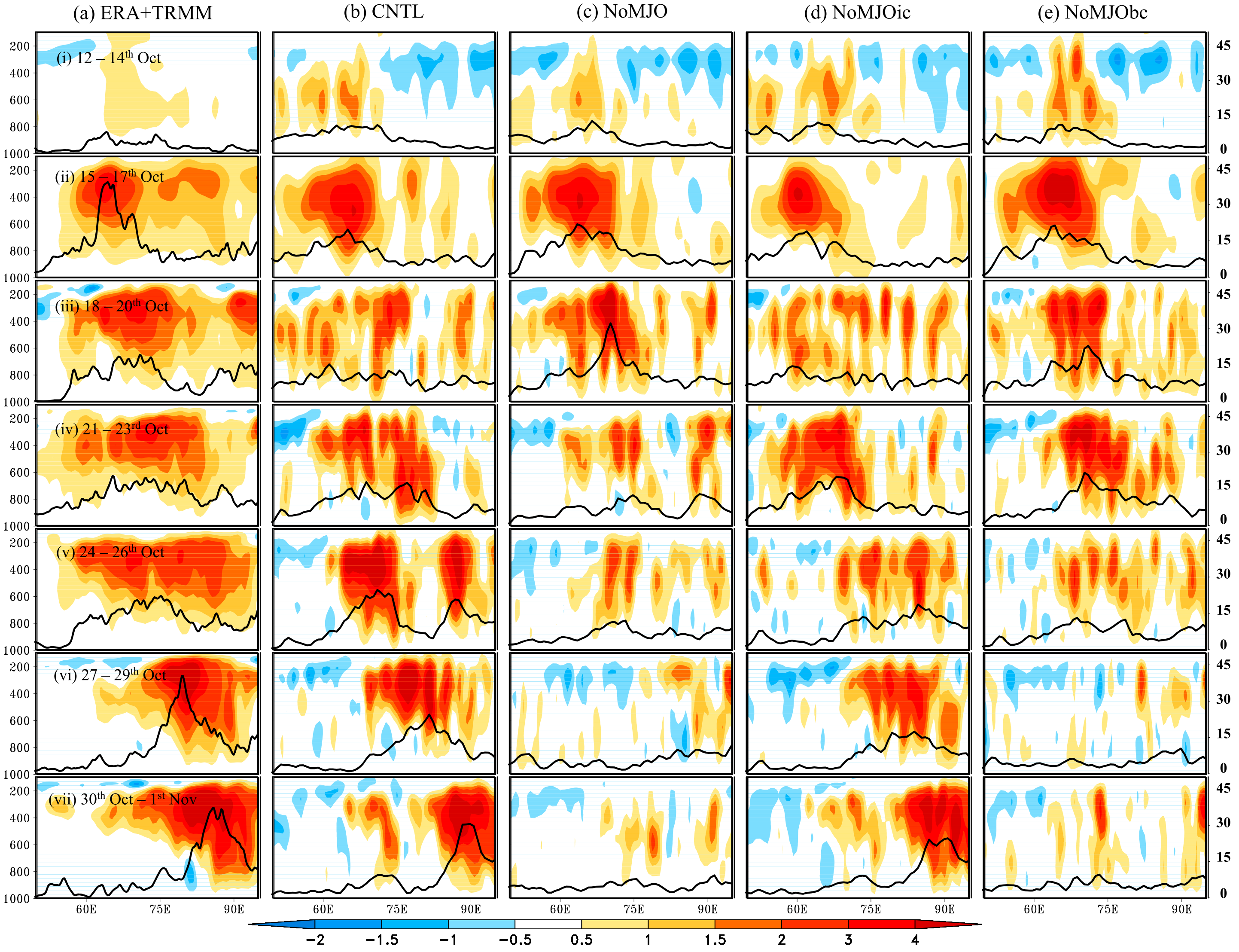

Figure 8. Longitude-pressure diagram of 3 day mean vertical velocity (cm s^{-1}; red shading: ascent and blue shading: descent) from 12 October to 1 November, for the October MJO event from (a) ERA-Interim vertical velocity and TRMM3B42 precipitation, (b) CNTL simulation, (c) NoMJO, (d) NoMJOic, and (e) NoMJObc experiments, respectively. Precipitation (mm/d) black curves with the vertical axes to the right are also shown. Vertical velocity and precipitation first averaged over the latitudes 5°S–5°N and a 150 km running averages along longitudes are also applied.

large-scale vertical velocity along with surface rainfall, averaged between the 5°S and 5°N, during 12 October to 1 November. Observation (Figure 8a) suggests suppressed convection over the Indian Ocean during 12–14 October, followed by a westward tilt and a top-heavy vertical motion profile during 15–17 October. Vertical structure of convection becomes more organized by 18–20 October; during 21–23 October, a top-heavy vertical velocity profile with a first baroclinic mode-like structure is collocated with the precipitation maxima between 67° and 75°E. Eastward of this region is mostly associated with a bottom-heavy shallow ascent profile, while westward of this region is dominated by a stratiform-like cloud structure. Overall, this structure of bottom-heavy ascents in the leading edge of the precipitation center, deep ascents collocated with the precipitation maxima, and ascent/descent trailing the maximum precipitation is maintained during the entire eastward propagation of the MJO event. In the CNTL (Figure 8b) and NoMJOic (Figure 8d) experiments, the suppressed convection over the Indian Ocean with a weak precipitation peak during 12–14 October followed by a westward tilted baroclinic structure of the vertical motions around 60°E with a precipitation maximum (~20 mm/d) during 15–17 October suggests the initiation of an MJO event. During 21–23 October, a rainfall maximum around 67°E–70°E is associated with a top-heavy vertical

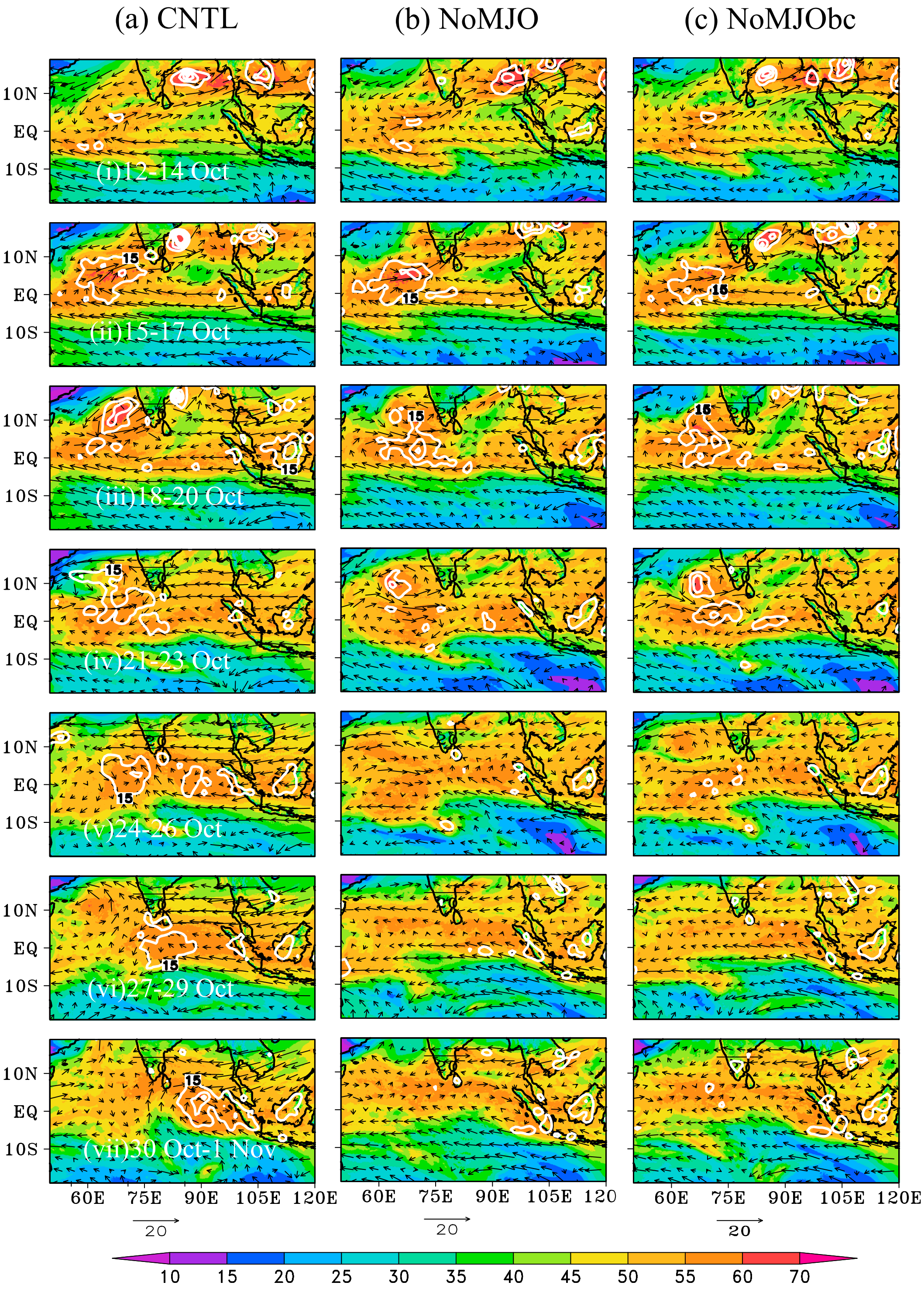

Figure 9. Spatial distribution of 3 day mean total precipitable water (shaded; mm), precipitation (white contours; 15, 30, 45, and 60 mm d^{-1}) and 850 hPa horizontal winds (vectors) from 12 October to 1 November, for the October MJO event, from (a) CNTL simulation and (b) NoMJO and (c) NoMJObc experiments, respectively.

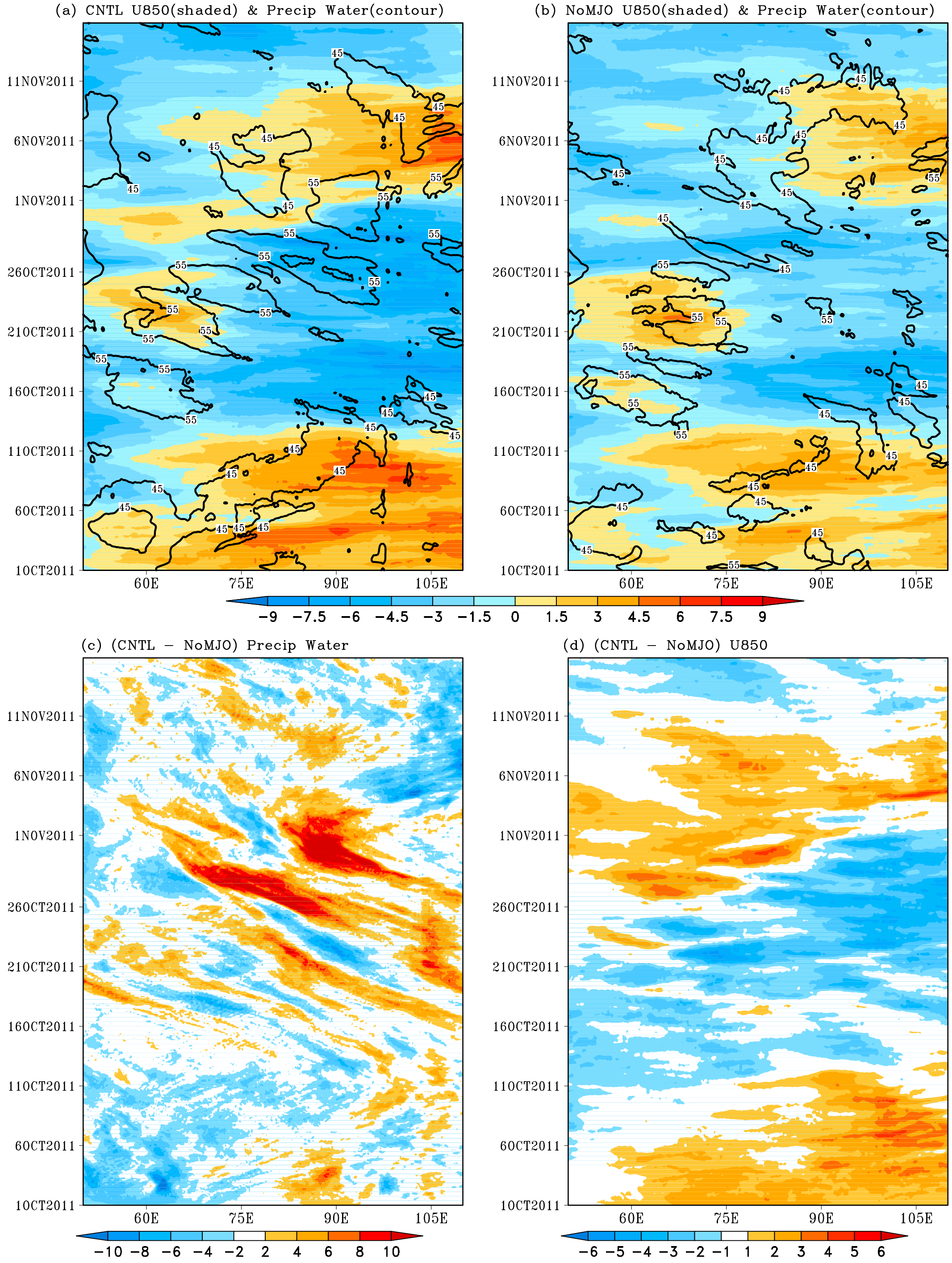

Figure 10. Time-longitude diagram of 850 hPa zonal wind (shaded; m s^{-1}) and total precipitable water (contour; for 45 and 55 mm) from (a) CNTL simulation and (b) NoMJO experiment. Bottom panels show the difference between the experiments (CNTL-NoMJO) for (c) precipitable water (mm) and (d) 850 hPa zonal wind. All the panels are averaged over the latitude 7°S–7°N, respectively.

velocity profile, while a bottom-heavy shallow ascent structure can be seen to the east. In general, this transition from shallow ascent to deep convection, where surface rainfall center is located, is well maintained during the eastward propagation of the MJO event. In summary, the eastward propagating MJO is reasonably well captured by both the CNTL and NoMJOic experiments (with the MJO signals retained in the boundary conditions) but not by either the NoMJO or NoMJObc experiment that filters out the global circumnavigating intraseasonal signals from the lateral boundary conditions. Next we will seek to identify the dynamical reasoning for the failure of the NoMJO and NoMJObc experiments specifically after 21 October.

3.2. Possible Causes for the MJO Failure in NoMJO and NoMJObc

Figure 9 depicts the corresponding horizontal distributions of the 3 day averaged total precipitable water content (shaded), 850 hPa wind vectors, and accumulated rainfall (contours) for each experiment, during 12 October to 1 November. The NoMJOic experiment is very similar to CNTL, so it is not shown here for brevity. Consistent with the vertical structure of vertical velocity (Figure 8), the horizontal distributions further suggest that the MJO propagation is only seen in CNTL. At the initiation stage (15–17 October), all experiment depicts a lower level convergence of easterly and westerly winds at ~60–65°E and between 0 and 5°N, advection of dry air from the India subcontinent and enhancement of the local moist static energy in the Arabian Sea. The subsequent evolution of the synoptic circulation differs noticeably among the simulations. While all three simulations show strong rotation (hence the Rossby waves) to the west of active convection, easterlies east of MJO convection persist in the CNTL simulation, but they are substantially weaker in both NoMJO and NoMJObc, e.g., 18–20 and 21–23 October, when convection is still active in the northern and equatorial Indian Ocean for CNTL. The differences in the circulations and the moistures (specifically below 5°S) are more prominent after 25 October onward. Comparison of panels (v) and (vi) in Figure 9 shows that weaker easterlies, between latitude 7°S to 7°N, in the east of convection in the NoMJO and NoMJObc experiments than CNTL, suggesting a weaker convergence and a weaker Kelvin wave activity in both experiments. This implies a weaker moisture transport in both NoMJO and NoMJObc to the east on convection after 25 October onward than CNTL. To quantify it more clearly, Figures 10a and 10b show the time longitude diagram of 850 hPa zonal wind along with the total precipitable water content averaged over 7°S–7°N in CNTL and NoMJO, respectively. The weaker easterlies east of 75°E after 18 October, more so after 21 October, are also associated with a lower moisture content. The difference (CNTL-NoMJO) of precipitable water (Figure 10c) and 850 hPa zonal wind (Figure 10d) not only demonstrates the weaker easterlies in the east of 75°E in NoMJO but also clearly suggests a stronger convergence and associated moister atmosphere in the CNTL simulation around 26 October onward (also east of 75°E). The relatively weaker easterlies in NoMJO indicate the absence of Kelvin waves, very likely since removal of the MJO signal from the boundaries weakens the large-scale circulation and moisture and hence the instability of the system which further reduces the chance of Kelvin waves to develop. Hence, the lack of the easterlies, which could advect relatively moist air and favor convergence at the leading edge of the westerlies, may be responsible for the diminishing MJO signatures in the two sensitivity experiments, NoMJO and NoMJObc.

The relatively dry air to the south of the equator may also be a possible cause for the MJO sensitivity in these sensitivity experiments. By 20 October onward the NoMJO and NoMJObc experiments show a development of dry air mass (lower precipitable water) east of 70°E and south of 10°S comparing to the CNTL simulation (Figure 9). This anomalously dry air mass is transported toward the equator by the trade wind that might weaken the instability of tropical atmosphere (Figure 9). The failure of eastward propagation in MJO convection by NoMJO and NoMJObc might be due to enhanced dry air transport by the southeasterlies toward the convergence region which prevents the buildup of moist static energy and consequent convection. To further quantify the above statement, we computed the 850 hPa moisture convergence and lower level (950–700 hPa) averaged moist static energy averaged over the region of 65°–95°E and 5°S–5°N; its time evolution is presented in Figure 11, which shows that at the time of MJO initiation (around 16 October 2011; marked by dashed line) both the moisture convergence (Figure 11a) and moist static energy (Figure 11b) are increasing in all experiments, even slightly higher in NoMJO and NoMJObc than CNTL and NoMJOic. However, from around 20 October onward the moisture convergence and moist static energy start to decrease in the NoMJO and NoMJObc experiments (instead of increasing in CNTL) that is associated with the transport of dry air (Figures 9 and 10). In consequence, convection starts to dissipate from 21 October onward instead of organization in the NoMJO and NoMJObc experiments.

Time evolutions of the vertical structures of zonal wind, vertical velocity, temperature anomaly, and relative humidity averaged over a central Indian Ocean box area (73–80°E and 0–5°N; collocated approximately with the DYNAMO northern sounding array or NSA) for the DYNAMO observations as well as in different sensitivity

(a) Moisture Convergence (g/kg/s)

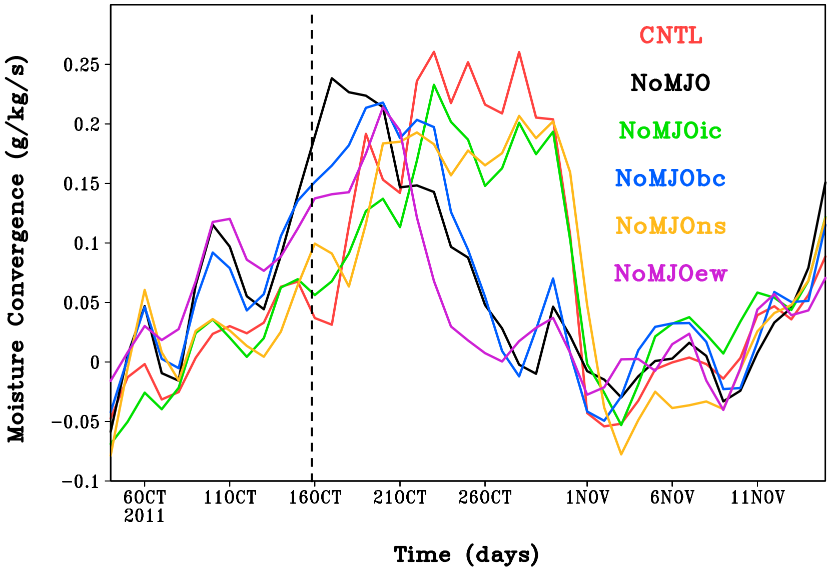

(b) Moist Static Energy (KJ/kg)

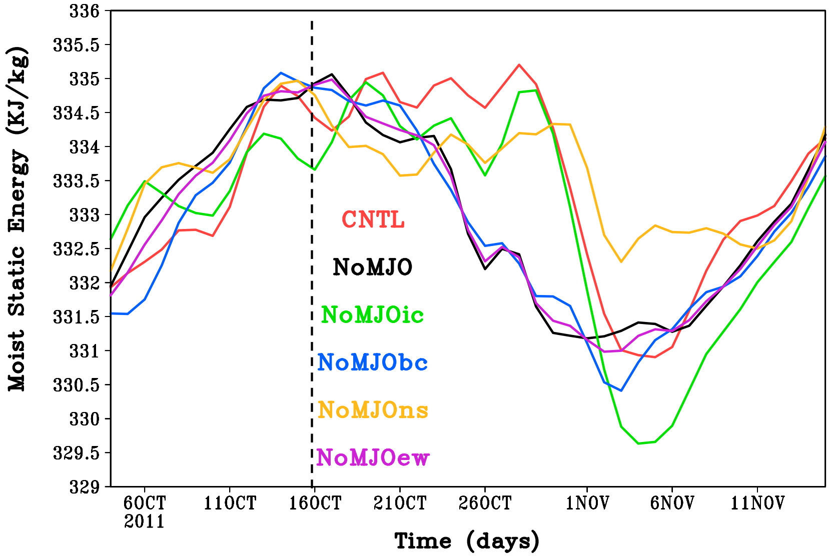

Figure 11. Time evolution of the (a) 850 hPa moisture convergence (g kg^{-1} s^{-1}) and (b) lower level (950–700 hPa) average moist static energy (KJ kg^{-1}) average over the region 65°–95°E and 5°S–5°N for CNTL simulation (red curve), NoMJO (black), NoMJOic (green), NoMJObc (blue), NoMJOns (yellow), and NoMJOew (purple) experiments, respectively. The dashed line around 16 October 2011 indicates the initiation of MJO in western Indian Ocean.

experiments are shown in Figure 12. The westerly wind burst at low levels is clearly seen in all the experiments at around 16 October consistent with the observation. During the first half of October, winds at lower levels (600–800 hPa) are dominated by westerlies, which become easterly just before the MJO initiation while turning back to westerlies at the later period of the active phase (i.e., late October to early November), as simulated in both the CNTL and NoMJOic experiments.

Consistent with Figure 8, vertical velocity has a top-heavy structure during the MJO active phases for both CNTL and NoMJOic in contrast to the NoMJO and NoMJObc experiments which fail to capture the same structure. The third row of Figure 12 shows the temperature anomalies computed by subtracting the time mean of temperature profiles averaged over central Indian Ocean box area. An initiation of a warmer

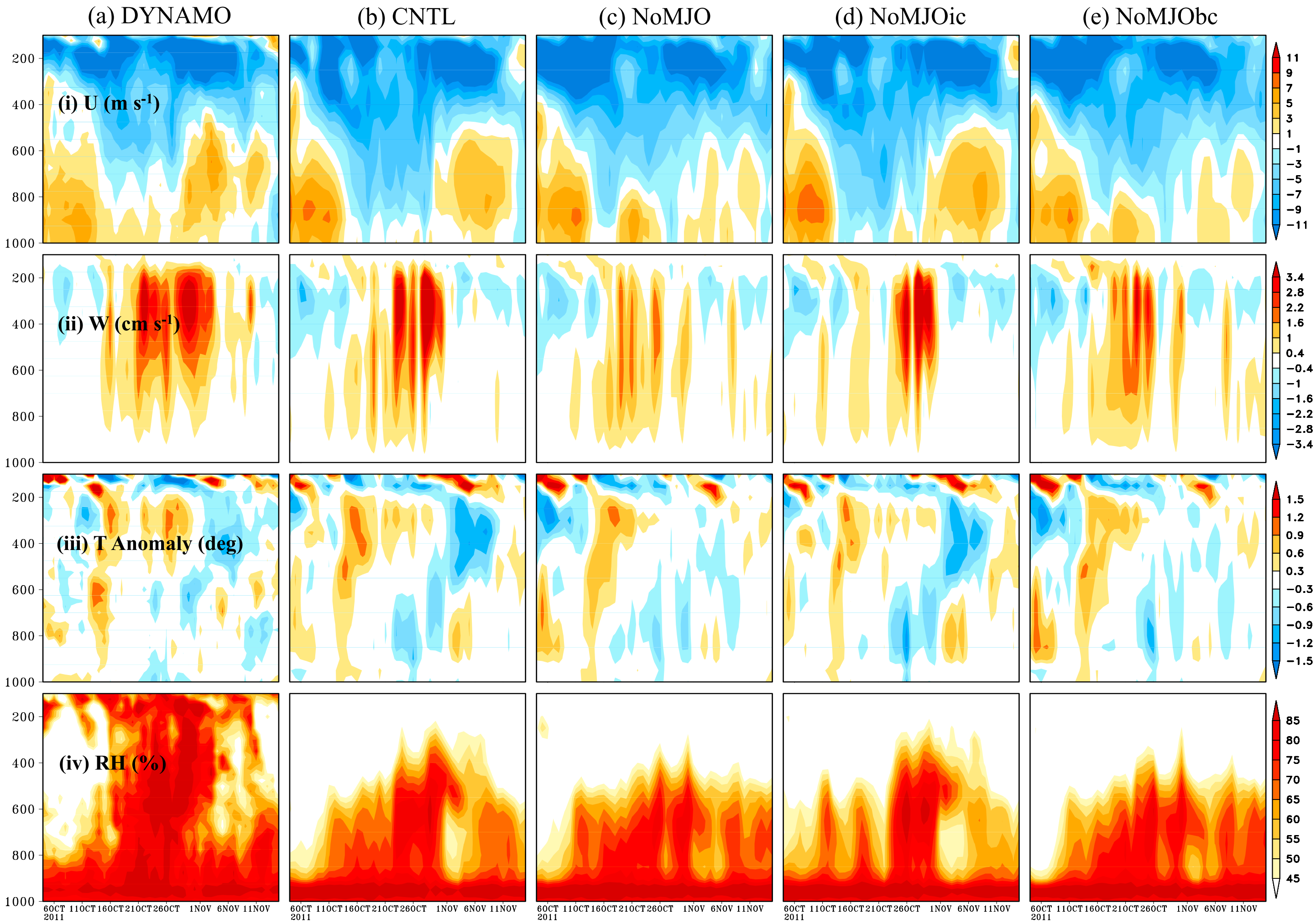

Figure 12. Time evolution of the area averaged (0°–5°N; 73°–80°E) vertical structure of (i) zonal wind (m s^{-1}), (ii) vertical motion (cm s^{-1}), (iii) temperature anomaly (°K), and (iv) relative humidity (%) for (a) DYNAMO observation, (b) CNTL simulations, (c) NoMJO, (d) NoMJOic, and (e) NoMJObc experiments respectively. Anomaly is computed with respect to their own 46 day climatology from each experiment.

temperature anomaly from the lower level during 10–15 October and its gradual extension to the upper troposphere during the active phase of MJO is consistent among all experiments but with varied magnitudes. However, an organized structure of colder temperature anomaly, extending from lower to upper troposphere, starting from the peak MJO strength (~26 October) is only depicted well in the CNTL and NoMJOic experiments, indicating transitioning of convective to stratiform clouds. Consistent with the zonal and vertical wind structure, the temperature structures are also depicted similarly in respect to the observational analysis in both CNTL and NoMJOic but not in the other two experiments (NoMJO and NoMJObc).

The steady increase of lower tropospheric moisture prior to the MJO event is shown in Figure 12 for both CNTL and NoMJOic, when the lower level easterly wind is associated with a positive temperature anomaly. Vertical advection of moisture by large-scale vertical motions moistens the upper levels, accompanying deeper convection during the active MJO phases. In general, Figure 12 suggests that lower levels lead the upper levels apparently for all variables (i.e., a westward tilt with height), which is consistent in simulations with a more coherent MJO structure (CNTL and NoMJOic). Both experiments with MJO signal filtered from the lateral boundary conditions (NoMJObc and NoMJO) fail to simulate the progression of the MJO from the lower to the upper troposphere and the distinct westward tilt structure over the NSA box region over the central Indian Ocean during the life cycle of the October MJO event in contrast to the CNTL and NoMJOic experiments.

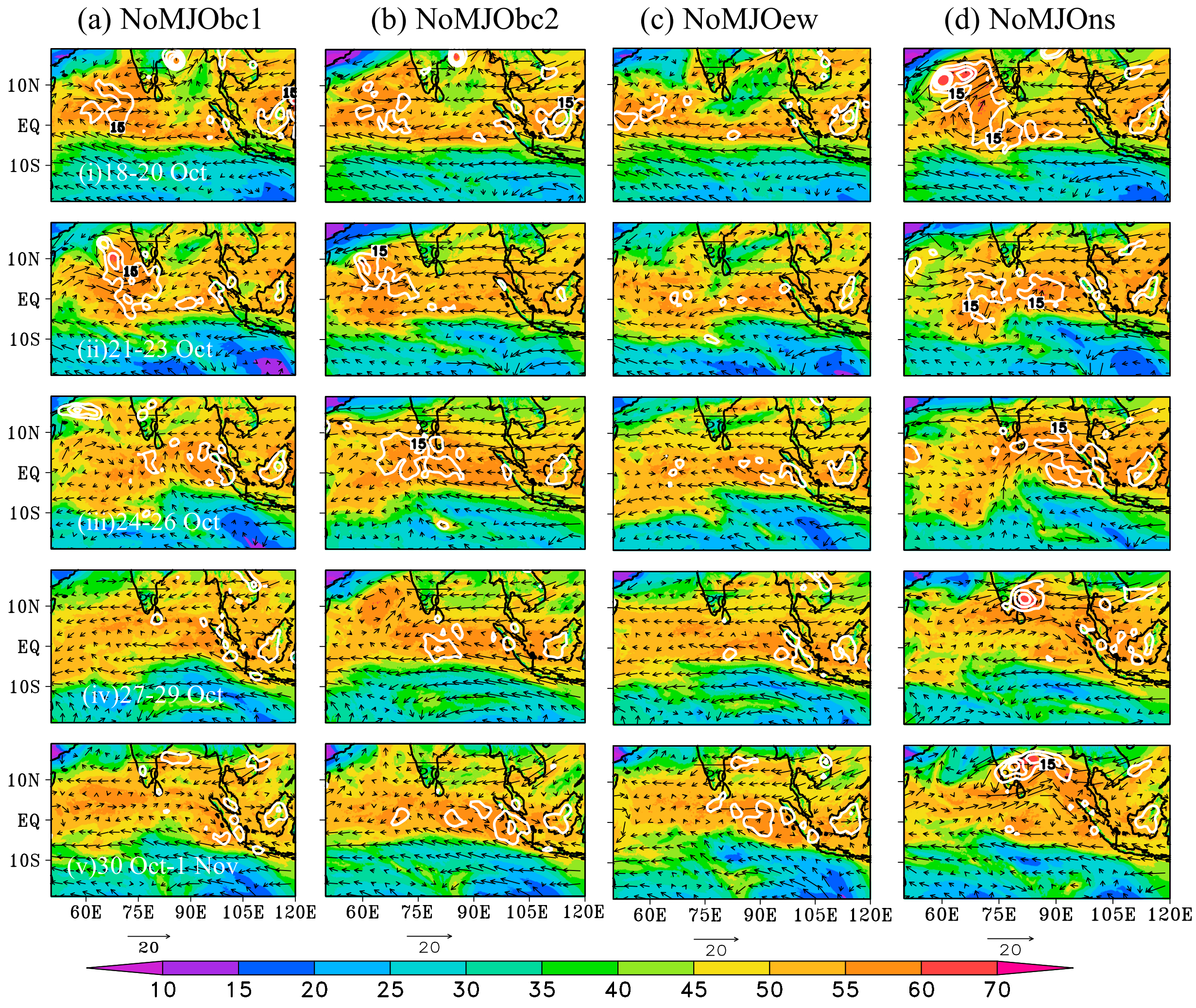

Figure 13. Spatial distribution of 3 day mean total precipitable water (shaded; mm), precipitation (white contours; 15, 30, 45, and 60 mm d^{-1}) and 850 hPa horizontal winds (vectors) for the propagation phase (18 October to 1 November) of October MJO event, from (a) NoMJObc1, (b) NoMJObc2, (c) NoMJOew, and (d)NoMJOns experiments, respectively.

3.3. Role of Boundary Conditions in MJO Propagation

To further quantify the importance of boundary conditions, two additional experiments are designed, similar to NoMJObc experiments but the MJO filter is applied on 16 October (NoMJObc1) and 26 October (NoMJObc2) onward instead of 1 October 2011 (Table 1). Both experiments are able to capture the initiation (not shown here since figure focuses mainly the propagation phase), but the NoMJObc1 experiment is not able to maintain organized convection after 23 October, indicating the weakening of MJO just after a few days of removing the MJO filtered signal from its lateral boundary conditions (Figure 13a). Failure to capture the MJO propagation in NoMJObc1 may be due to the weaker easterlies to the east of convection (or weaker Kelvin wave activity) after 25 October and also to development of dry air mass east of 70°E and south of 10°S, similar to the NoMJO and NoMJObc experiments, and its associated transport toward the equator by the trade wind. This dry air advection may significantly reduce moist static energy in the equatorial Indian Ocean and dissipates the MJO convection after 24 October. In contrast, experiment NoMJObc2 (Figure 13b) is able to capture the MJO initiation and propagation similar to the CNTL simulation, and also, the anomalously moist air mass can be seen in the above mentioned region as compared to NoMJO (Figure 9b), NoMJObc (Figure 9c), and NoMJObc1 (Figure 13a) specifically during 18–29 October. The contrasts in the NoMJObc1 and NoMJObc2 experiments also clearly suggest that boundary conditions play an important role to initiate and propagate the MJO during the dry phase over the West Indian Ocean.

Next, we seek to further assess the relative importance of east-west propagation mode in support to our importance of circumnavigating signal. We perform two additional experiments, similar to NoMJO, but where the MJO filter is only applied in the east-west boundary (NoMJOew) in contrast to NoMJOns in which the MJO filter applied only in the north-south boundary (Table 1).

Figures 13c and 13d show that there is little or no initiation and propagation of the MJO structure in the NoMJOew experiment, compared to a strong and easily identifiable MJO mode in the NoMJOns experiment (though with slightly faster eastward propagation and somewhat a northward shift compared to CNTL). The failure of MJO convection is caused by the drier atmosphere in the southern and western boundaries (Figure 2), followed by the weaker easterlies (Figure 10) and absence of Kelvin wave, which weakens the moisture transport and hence moist instability (Figure 11) in the NoMJOew experiment compared to NoMJOns. This experiment further supports our finding that boundary conditions are mostly dominated by the east-west propagating circumnavigating MJO signal instead of the extratropical influences from the north-south boundaries. However, interactions between the global circumnavigating signal and the extratropical signals may have also played some roles through the western boundary in modulating the position, strength, and phase speed of the current MJO event as seen in the difference between CNTL and NoMJOns. These interactions might have also been even more important in the longitude ranges that are beyond the current regional domain. Such interactions could be an interesting topic for future research.

4. Concluding Remarks

This study using a regional-scale convection-permitting model gives a conclusive evidence that a global circumnavigating MJO mode propagating through the east-west lateral boundary conditions over the Indian Ocean. This study for the first time demonstrates uniquely the predominant role of a global circumnavigating mode in the initiation and propagation of the October 2011 MJO event occurred during the DYNAMO field campaign. Sensitivity experiments also show that the global dry MJO signals passing through the east-west boundaries are far more important than the extratropical influences from the north-south boundaries.

Without the global mode passing through the lateral boundary conditions, there are still strong convective activities in the simulation domain, initiated in the western Indian Ocean at the time of observed MJO initiation but little to no propagation is simulated. While all the simulations show a strong rotational circulation, the lack of the easterlies to the east of the active convection in the sensitivity experiments suggests that a relatively weaker Kelvin wave could have reduced advection of moist air from the east and weakens the lower level convergence. This study succinctly demonstrates that when the “global circumnavigating modes” are removed from the western boundary conditions (Figure 2), anomalous westerlies (Figure 10d) are associated with reduced low-level moisture convergence (Figure 11a) and hence failed MJO initiation/propagation in the NoMJO, NoMJObc, and NoMJOew experiments.

Meanwhile, for the same regional domain started 2 weeks earlier the commencement of MJO event, there is little impact of whether or not the global MJO signals retained in the initial conditions. Also worth noting is that simulations that represent well the propagating MJOs can also simulate better the westward propagating inertial gravity waves coupled with moist convection during active segment of MJO. It is not yet clear whether or not the abundant coincident westward propagating inertial gravity waves play any roles in the success of MJO simulations might be an exciting area for future research to examine their causality.

Mechanism-denial experiments have been conducted in the past [*Ma and Kuang*, 2016; *Hall et al.*, 2017; *Ray and Li*, 2013] through identifying and disabling the respected processes in the model and evaluated their responses to the MJO simulations. Turning on and off these processes might interfere with the mean state which motivates *Ma and Kuang* [2016] to exclude the role of mean state changes when the influence of extratropical forcings is examined using a superparameterized community atmospheric model. These mechanism-denial experiments were also performed by modifying the boundary conditions of numerical models either by removing different time scales [*Hall et al.*, 2017] or by modifying the east-west to north-south lateral boundaries [*Ray and Li*, 2013]. *Hall et al.* [2017] found that removing the intraseasonal time scale from the boundary conditions, half of the intraseasonal variance can be attributed to boundary influence and specifically to the presence of intraseasonal extratropical signal. Comparing the impact of east-west versus north-south boundary conditions using an atmospheric general circulation model, *Ray and Li* [2013] found that the extratropical forcings influence more on the circumnavigating signal for the MJO variances. On the contrary, the current study on the predominant role of the circumnavigating signal in the MJO initiation and propagation is consistent with many other earlier studies [e.g., *Ajayamohan et al.*, 2013; *Matthews*, 2008; *Kikuchi and Takayabu*, 2003].

Note that the current study deals with a convection-permitting simulation of a real-world MJO event (October MJO event in 2011) while only large-scale MJO-like disturbances in the European Centre/Hamburg-4 model are examined in *Ray and Li* [2013]. The current work also contrasts from the *Hall et al*. [2017] which filtered only the temporal scale (20–100 days) that may have not separate out part of the Rossby wave signals from the MJO. Nevertheless, the predominant role of the global circumnavigating signal found for the 2011 October MJO event in the regional model domain over the Indian Ocean found in this study does not preclude the possibilities of interactions with and influences of midlatitude disturbances with the tropical MJO elsewhere. More detailed studies remain needed to clarify these interactions and influences.

Acknowledgments
Current research is primarily sponsored by NSF grants 1305798 and 1305788 and NASA grant NNX12AJ79G. Discussions with Adam Sobel, Chidong Zhang, and many other were beneficial. The authors acknowledge data and modeling help from Yonghui Weng, Juan Fang, Yue (Michael) Ying, and Christopher Melhauser. Comments from anonymous reviewers are very beneficial. The authors acknowledge the Texas Advanced Computing Center (TACC) at The University of Texas at Austin for providing computing and storage resources that have contributed to the research results reported within this paper. All data presented are stored and can be accessed through the TACC data archive (http://www.tacc.utexas.edu).

References

Ajayamohan, R. S., B. Khouider, and A. J. Majda (2013), Realistic initiation and dynamics of the Madden-Julian Oscillation in a coarse resolution aquaplanet GCM, *Geophys. Res. Lett.*, *40*, 6252–6257, doi:10.1002/2013GL058187.

Chi, Y., F. Zhang, W. Li, J. He, and Z. Guan (2015), Correlation between the onset of the east Asian subtropical summer monsoon and the eastward propagation of the Madden–Julian Oscillation, *J. Atmos. Sci.*, *72*, 1200–1214.

Dee, D. P., et al. (2011), The ERA-Interim reanalysis: Configuration and performance of the data assimilation system, *Q. J. R. Meteorol. Soc.*, *137*, 553–597, doi:10.1002/qj.828.

Fang, J., and F. Zhang (2016), Contribution of tropical waves to the formation of super typhoon Megi (2010), *J. Atmos. Sci.*, *73*, 4387–4405.

Fu, X., W. Wang, J.-Y Lee, B. Wang, K. Kikuchi, J. Xu, J. Li, and S. Weaver (2015), Distinctive roles of air–sea coupling on different MJO events: A new perspective revealed from the DYNAMO/CINDY field campaign, *Mon. Weather Rev.*, *143*, 794–812.

Gustafson, W. I., and B. C. Weare (2004a), MM5 modeling of the Madden-Julian Oscillation in the Indian and West Pacific Oceans: Model description and control run results, *J. Clim.*, *17*, 1320–1337.

Gustafson, W. I., and B. C. Weare (2004b), MM5 modeling of the Madden-Julian Oscillation in the Indian and West Pacific Oceans: Implications of 30–70 day boundary effects on MJO development, *J. Clim.*, *17*, 1338–1351.

Hall, N. M. J., S. Thaibaut, and P. Marchesiello (2017), Impact of the observed extratropics on climatological simulations of the MJO in a tropical channel model, *Clim. Dyn.*, *48*, 2541–2555, doi:10.1007/s00382-016-3221-5.

Hoskins, B. (2013), The potential for skill across the range of the seamless weather-climate prediction problem: A stimulus for our science, *Q. J. R. Meteorol. Soc.*, *139*, 573–584, doi:10.1002/qj.1991.

Huffman, G. J., R. F. Adler, D. T. Bolvin, G. Gu, E. J. Nelkin, K. P. Bowman, Y. Hong, E. F. Stocker, and D. B. Wolff (2007), The TRMM multi-satellite precipitation analysis: Quasi-global, multi-year, combined-sensor precipitation estimates at fine scale, *J. Hydrometeorol.*, *8*, 38–55.

Hung, M.-P., J.-L. Lin, W. Wang, D. Kim, T. Shinoda, and S. J. Weaver (2013), MJO and convectively coupled equatorial waves simulated by CMIP5 climate models, *J. Clim.*, *26*, 6185–6214, doi:10.1175/JCLI-D-12-00541.1.

Jiang, X., et al. (2015), Vertical structure and physical processes of the Madden-Julian Oscillation: Exploring key model physics in climate simulations, *J. Geophys. Res. Atmos.*, *120*, 4718–4748, doi:10.1002/2014JD022375.

Johnson, R. H., P. E. Ciesielski, J. H. Ruppert, and M. Katsumata (2015), Sounding-based thermodynamic budgets for DYNAMO, *J. Atmos. Sci.*, *72*, 598–622, doi:10.1175/jas-d-14-0202.1.

Kikuchi, K., and Y. N. Takayabu (2003), Equatorial circumnavigation of moisture signal associated with the Madden-Julian Oscillation (MJO) during boreal winter, *J. Meteorol. Soc. Jpn.*, *81*, 851–869.

Knutson, T. R., and K. M. Weickmann (1987), 30–60 day atmospheric oscillations: Composite life cycles of convection and circulation anomalies, *Mon. Weather Rev.*, *115*, 1407–1436.

Lau, K. M., and L. Peng (1987), Origin of low-frequency (intraseasonal) oscillations in the tropical atmosphere. Part I: Basic theory, *J. Atmos. Sci.*, *44*, 950–972.

Lin, J.-L., B. E. Mapes, M. Zhang, and M. Newman (2004), Stratiform precipitation, vertical heating profiles, and the Madden-Julian Oscillation, *J. Atmos. Sci.*, *61*, 296–309.

Lin, J.-L., et al. (2006), Tropical intraseasonal variability in 14 IPCC AR4 climate models. Part I: Convective signals, *J. Clim.*, *19*, 2665–2690, doi:10.1175/JCLI3735.1.

Ma, D., and Z. Kuang (2016), A mechanism-denial study on the Madden-Julian Oscillation with reduced interference from mean state changes, *Geophys. Res. Lett.*, *6*, 2989–2997, doi:10.1002/2016GL067702.

Madden, R. A., and P. R. Julian (1971), Detection of a 40–50 day oscillation in the zonal wind in the tropical Pacific, *J. Atmos. Sci.*, *28*, 702–708.

Madden, R. A., and P. R. Julian (1972), Description of global-scale circulation cells in tropics with a 40–50 day period, *J. Atmos. Sci.*, *29*, 1109–1123.

Maloney, E. D., and B. O. Wolding (2015), Initiation of an intraseasonal oscillation in an aquaplanet general circulation model, *J. Adv. Model. Earth Syst.*, *7*, 1956–1976, doi:10.1002/2015MS000495.

Maloney, E. D., A. H. Sobel, and W. M. Hannah (2010), Intraseasonal variability in an aquaplanet general circulation model, *J. Adv. Model. Earth Syst.*, *2*, 5, doi:10.3894/JAMES.2010.2.5.

Matthews, A. J. (2008), Primary and successive events in the Madden–Julian Oscillation, *Q. J. R. Meteorol. Soc.*, *13*, 439–453.

Pritchard, M. S., and C. S. Bretherton (2014), Causal evidence that rotational moisture advection is critical to the superparameterized Madden-Julian Oscillation, *J. Atmos. Sci.*, *71*(2), 800–815, doi:10.1175/JAS-D-13-0119.1.

Ray, P., and T. Li (2013), Relative roles of circumnavigating waves and extratropics on the MJO and its relationship with the mean state, *J. Atmos. Sci.*, *70*, 876–893.

Ray, P., and C. Zhang (2010), A case study of the mechanics of extratropical influences on the initiation of MJO, *J. Atmos. Sci.*, *67*, 515–528.

Ray, P., C. Zhang, J. Dudhia, and S. S. Chen (2009), A numerical case study on the initiation of the Madden-Julian Oscillation, *J. Atmos. Sci.*, *66*, 310–331.

Schreck, C. J., J. Molinari, and K. I. Mohr (2011), Attributing tropical cyclogenesis to equatorial waves in the western North Pacific, *J. Atmos. Sci.*, *68*, 195–209.

Schreck, C. J., J. Molinari, and A. Aiyyer (2012), A global view of equatorial waves and tropical cyclogenesis, *Mon. Weather Rev.*, *140*, 774–788, doi:10.1175/MWR-D-11-00110.1.

Seo, K.-H., W. Wang, J. Gottschalck, Q. Zhang, J.-K. E. Schemm, W. R. Higgins, and A. Kumar (2009), Evaluation of MJO forecast skill from several statistical and dynamical forecast models, *J. Clim.*, *22*, 2372–2388.

Skamarock, W. C., J. B. Klemp, J. Dudhia, D. O. Gill, D. M. Barker, M. G. Duda, X.-Y. Huang, W. Wang, and J. G. Powers (2008), A description of the Advanced research WRF version 3, *NCAR Tech. Note NCAR/TN-475+STR*, 125 pp.

Sobel, A. H., and E. D. Maloney (2012), An idealized semi-empirical framework for modeling the Madden-Julian Oscillation, *J. Atmos. Sci.*, *69*(5), 1691–1705, doi:10.1175/JAS-D-11-0118.1.

Sobel, A. H., E. D. Maloney, G. Bellon, and D. M. Frierson (2010), Surface fluxes and tropical intraseasonal variability: A reassessment, *J. Adv. Model. Earth Syst.*, *2*, 2, doi:10.3894/JAMES.2010.2.2.

Sobel, A. H., S. Wang, and D. Kim (2014), Moist static energy budget of the MJO during DYNAMO, *J. Atmos. Sci.*, *71*, 4276–4291.

Wang, S., A. H. Sobel, and Z. Kuang (2013), Cloud-resolving simulation of TOGA-COARE using parameterized large-scale dynamics, *J. Geophys. Res. Atmos.*, *118*, 6290–6301, doi:10.1002/jgrd.50510.

Wang, S., A. H. Sobel, F. Zhang, Y. Sun, Y. Yue, and L. Zhou (2015), Regional simulation of the October and November MJO events observed during the CINDY/DYNAMO field campaign at gray zone resolution, *J. Clim.*, *28*, 2097–2119.

Wang, S., A. H. Sobel, and J. Nie (2016), Modeling the MJO in a cloud-resolving model with parameterized large-scale dynamics: Vertical structure, radiation, and horizontal advection of dry air, *J. Adv. Model. Earth Syst.*, *8*, 121–139, doi:10.1002/2015MS000529.

Wedi, N. P., and P. K. Smolarkiewicz (2010), A nonlinear perspective on the dynamics of the MJO: Idealized large eddy simulations, *J. Atmos. Sci.*, *67*, 1202–1217.

Wheeler, M., and G. N. Kiladis (1999), Convectively coupled equatorial waves: Analysis of clouds and temperature in the wavenumber–frequency domain, *J. Atmos. Sci.*, *56*, 374–399.

Yoneyama, K., C. Zhang, and C. N. Long (2013), Tracking pulses of the Madden-Julian Oscillation, *Bull. Am. Meteorol. Soc.*, *94*, 1871–1891.

Zhang, C. (2005), Madden-Julian Oscillation, *Rev. Geophys.*, *43*, RG2003, doi:10.1029/2004RG000158.

Zhao, C., T. Li, and T. Zhou (2013), Precursor signals and processes associated with MJO initiation over the tropical Indian Ocean, *J. Clim.*, *26*, 291–307, doi:10.1175/JCLI-D-12-00113.1.